CrossMark

A Tale of Three Dust Populations: Variable R_V and Extreme Polarization along Sight Lines toward ζ Ophiuchi

Ashley N. Piccone 🄳 and Henry A. Kobulnicky 🄳
University of Wyoming, 1000 E. University Ave., Laramie, WY 82071, USA; chipk@uwyo.edu
Received 2021 April 16; revised 2021 October 25; accepted 2021 October 26; published 2022 January 19

Abstract

Dust permeates the interstellar medium, reddening and polarizing background starlight, but dust properties vary with local environment. In order to characterize dust in a highly irradiated diffuse cloud, we measure the reddening and optical polarization toward 27 stars surrounding the midlatitude $b = +24°$ O9.2IV star ζ Ophiuchi, using new optical spectroscopy and polarimetry. We incrementally deredden and depolarize with distance, allowing us to distinguish dust components along these sight lines. The data indicate three distinct dust populations: a foreground component characteristic of average Milky Way dust ($R_V \approx 3.1$, $d \lesssim 180$ pc), a highly polarizing mid-distance component in the vicinity of ζ Oph ($R_V \approx 2.4$, 200 pc $< d <$ 300 pc), and a nonpolarizing distant component ($R_V \approx 3.6$, 600 pc $< d <$ 2000 pc). Prominent 8 μm infrared striations spanning the field of view likely have high polycyclic aromatic hydrocarbon content and are illuminated by ζ Oph. Foreground-subtracted polarizations roughly align with these striations, which, we argue, lie immediately behind ζ Oph and constitute the highly polarizing mid-distance dust. This component polarizes very efficiently ($P_V > 9.1E(B − V)$), implying a high degree of grain alignment and suggesting that the bulk of the polarization occurs in a small fraction of the volume. The large R_V in the distant component reveals that dust above the Galactic plane ($z > 250$ pc) may contain a greater fraction of large grains than the Milky Way average.

1. Introduction

Dust is an integral component of the interstellar medium (ISM), infiltrating signals from both Galactic and extragalactic objects. Interstellar dust extincts and reddens background light, necessitating corrections in most astronomical observations. Dust grains range in size depending on the environment and are thought to follow a power-law distribution as the result of formation and destruction processes (Clayton et al. 2003). Precise corrections for dust depend on understanding not only its spatial distribution but also the grain size distribution and its extinction properties in all three dimensions. All-sky infrared dust maps, like those from Schlegel et al. (1998) and Schlafly & Finkbeiner (2011), provide a low-resolution image of dust distribution in the Milky Way. Schlafly et al. (2017) and Green et al. (2019) have revealed dust populations as a function of Galactic position and distance. However, these dust maps are not capable of revealing how grain properties vary as a function of local environments, nor have they completely constrained how those properties may change above the Galactic plane.

Dust is often characterized by its extinction in magnitudes at V band (A_V) and ratio of interstellar extinction to reddening (R_V). The two quantities are related by $A_V = R_V E(B − V)$, where $E(B − V)$ is the color excess or reddening. The average R_V in the Milky Way is ≈ 3.1 (Schultz & Wiemer 1975). Larger R_V indicates an abundance of large dust grains, while a smaller R_V indicates a shift toward smaller dust grains (Mathis & Wallenhorst 1981). The transition between dense and diffuse clouds at $A_V \approx 3.2$ mag corresponds to a transition in R_V as

well: dense clouds have large R_V (3.5–4.0), while diffuse clouds have small or near-average R_V (Whittet et al. 2001). Large-R_V clouds show a reduction in the number of small dust grains, possibly as a result of aggregation of small particles in dense environments (Kim & Martin 1996). In diffuse cloud environments, ultraviolet photons may alter the grain size distribution in the opposite sense, leading to a small R_V through the destruction and fragmentation of large grains (Aannestad 1995). Many studies using coarse maps of interstellar reddening (e.g., Green et al. 2019) to correct for dust assume $R_V \approx 3.1$ and therefore do not account for dust properties that may vary by sight line or even with distance along a single sight line.

While dust properties like A_V and R_V can be measured with photometry and spectrophotometry, optical polarimetry of background stars provides another tool to probe the size, orientation, and alignment of grains. Hiltner (1949) and Hall (1949) first discovered that dust polarizes background starlight, which is a consequence of nonspherical dust grains aligned perpendicular to the interstellar magnetic field (Davis & Greenstein 1951). Radiative torques (RATs) have emerged as the dominant theory for grain alignment. RAT theory suggests that helical dust grains are spun up by an anisotropic radiation field so that their long axes are perpendicular to the magnetic field (Lazarian & Hoang 2007). A larger fraction of dust grains are aligned and create a more polarized signal when the ambient radiation is along magnetic field lines (Andersson et al. 2011). Grain alignment is therefore likely enhanced near radiation sources having high specific intensity (Andersson et al. 2015).

The mechanism of grain alignment depends on the size and composition of dust grains and the radiative environment. By studying the dark star-forming cloud ρ Ophiuchi in far-infrared
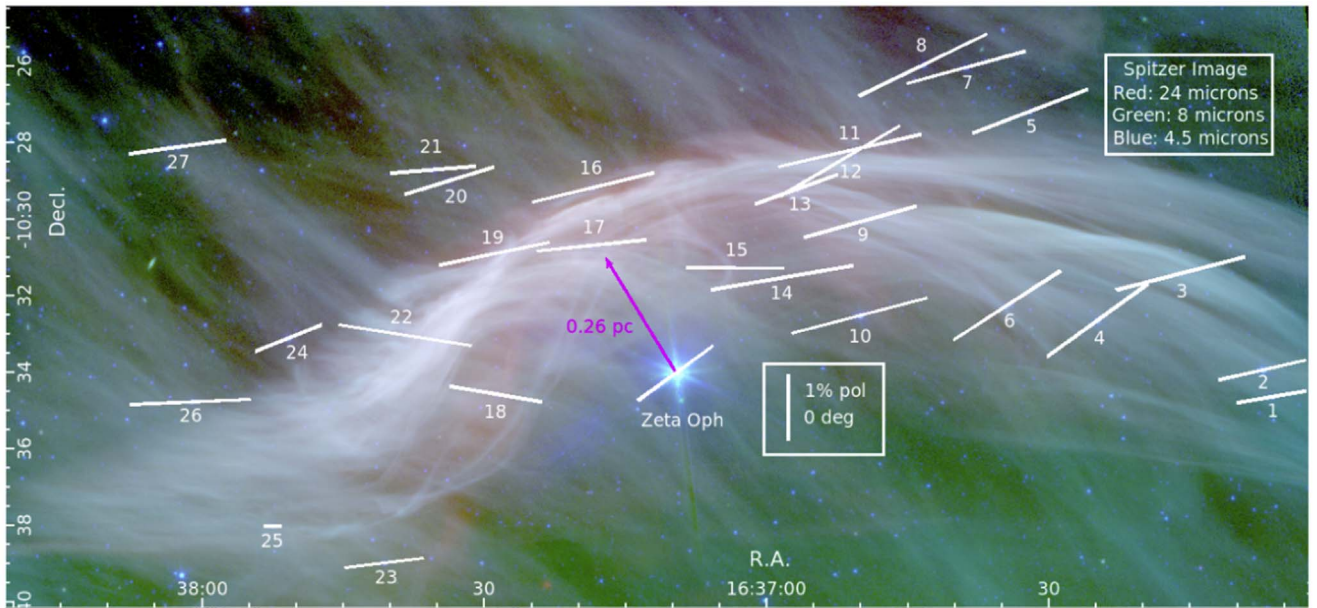
Figure 1. The ζ Oph field from Spitzer 24 μm, 8 μm, and 4.5 μm images. The bow shock nebula precedes the star and has a high surface brightness. At a distance of 182 pc, the apex of the nebula is a projected 0.26 pc from ζ Oph. The magenta vector shows this distance and the direction of the star's motion. Fainter dust striations span the entire field of view and are best traced in green (8 μm). White vectors show P_V and P.A. relative to the $P_V = 1\%$ and P.A. $= 0°$ legend. Numbers next to each vector provide the target identifier as in Table 1.

emission, Santos et al. (2019) discovered that polarization fraction decreases with increasing column density (and hence extinction), possibly due to increased magnetic field disorder or a loss of alignment efficiency deep within clouds. They proposed that warm dust grains at the outskirts of clouds are aligned through RAT while inner cold grains are shielded. While all grain alignment mechanisms fail at the center of dark clouds, those with smaller extinctions are expected to show more efficient alignment (Lazarian et al. 1997).

The high space velocity, hot, O9.2IV star ζ Ophiuchi makes an interesting laboratory for examining extinction and polarization along sight lines through a diffuse high-radiation environment. Because it is nearby, is at moderate Galactic latitude ($b = +24°$), and has a well-characterized foreground (Serkowski et al. 1975; Tachihara et al. 2000; Liszt et al. 2009; Choi et al. 2015; Siebenmorgen et al. 2020), the field of view around the star allows for relatively unconfused measurements of dust properties with distance. Hipparcos parallax measurements place ζ Oph at a distance of 112 pc (van Leeuwen 2007), but more recent estimates from Gaia suggest a distance of 182^{+53}_{-34} pc (Bailer-Jones et al. 2018). Because ζ Oph has an $m_G = 2.46$, it falls into a regime in which Gaia distances may have large systematic errors (Drimmel et al. 2019). However, Siebenmorgen et al. (2020) used two other distance estimates, the Ca II distance scale and the spectrophotometric distance, to calculate distances of 230^{+8}_{-12} pc. We will adopt a distance of 182^{+53}_{-34} pc for the remainder of this work. Figure 1 illustrates the ζ Oph region and reveals the prominent dust structures in infrared images from the Spitzer Space Telescope (Spitzer). Red/green/blue represent 24/8/4.5 μm, respectively. ζ Oph is preceded by a high surface brightness bow shock nebula, first discovered by Gull & Sofia (1979) in Hα at a standoff distance of 299″ or 0.26 pc at the adopted distance of 182 pc (Kobulnicky et al. 2019). The high proper motion of ζ Oph is parallel to the symmetry axis of the bow shock nebula and is shown by the magenta vector in Figure 1. Fainter infrared dust

structures also span the Spitzer image. These striations align approximately perpendicular to the bow shock structure and parallel to the peculiar motion of ζ Oph. The relationship between the fainter striations in Figure 1 and the bow shock nebula is unclear. The striations are large and extend much farther than the bow shock itself and well beyond the pictured field of view. These dust structures—the striations and the bow shock—are large in angular size, making them both interesting and easily accessible for investigating A_V, R_V, and polarization through this diffuse, high-radiation environment.

This work investigates the reddening and polarization along lines of sight in the high-radiation, diffuse environment surrounding ζ Oph in order to identify and characterize dust populations in that field as a function of distance. Section 2 introduces new spectrophotometry from the Apache Point Observatory (APO), optical polarimetry from the Wyoming Infrared Observatory (WIRO), and data reduction. Section 3 presents the spectral types, reddening estimates, and polarizations toward 27 background stars. Using available photometry in conjunction with our observations, we identify three primary dust structures located at various distances in the field of view. Section 4 explores the three dust populations and their relationships to the projected magnetic field and infrared striations. In Section 5, we summarize the conclusions from this investigation.

2. Observations and Data Reduction

We selected stars in close angular proximity to ζ Oph that were accessible to the observational limits of spectroscopy and polarimetry on a 2–4 m telescope. This resulted in 27 target stars both directly behind the bow shock nebula and in the surrounding field, with magnitudes $m_f \leqslant 15.2$, where m_f is the UCAC4 catalog optical photographic fit model magnitude (Zacharias et al. 2013). Table 1 lists basic data for the 27 targets. Column (1) provides the target number that is referenced throughout this paper. Column (2) lists the Gaia

Table 1
Targets Observed in the ζ Ophiuchi Field

Target	Gaia ID	R.A. (deg)	Decl. (deg)	m_f (mag)	m_V (mag)	d (pc)
ζ Oph	4337352305315545088	249.2875	−10.5669	⋯	2.56	182^{+53}_{-34}
1	4338102545907455744	249.0266	−10.5774	13.18	13.08	$436.1^{+7.9}_{-9.1}$
2	4338102722003440000	249.0303	−10.5656	13.01	13.21	2819^{+358}_{-287}
3	4338103271759259392	249.0668	−10.5238	14.55	14.51	3019^{+265}_{-227}
4	4338102923864645120	249.1036	−10.5442	11.84	11.90	$224.0^{+1.1}_{-2.0}$
5	4338108288281067264	249.1334	−10.4531	13.85	14.05	$423.3^{+4.7}_{-5.3}$
6	4338103684076094464	249.1438	−10.5379	13.33	13.38	$252.2^{+0.8}_{-2.2}$
7	4338108460079758336	249.1620	−10.4341	14.68	14.94	8434^{+2077}_{-1480}
8	4338128972843559808	249.1805	−10.4329	14.43	14.69	2420^{+197}_{-170}
9	4338104199472164352	249.2086	−10.5013	13.86	13.94	$435.5^{+4.6}_{-5.5}$
10	4338103507980197248	249.2088	−10.5421	12.74	13.13	1294^{+68}_{-63}
11	4338104405630603904	249.2136	−10.4704	14.61	14.97	$278.3^{+2.6}_{-2.5}$
12	4338104405630602240	249.2170	−10.4745	15.10	15.49	3247^{+482}_{-375}
13	4338104126455487488	249.2367	−10.4871	12.23	12.32	$427.6^{+6.4}_{-6.6}$
14	4337353404830237056	249.2431	−10.5256	14.67	14.72[a]	$489.2^{+7.3}_{-7.1}$
15	4337353370470494464	249.2637	−10.5214	14.80	15.07[a]	2500^{+223}_{-190}
16	4337377181769178752	249.3271	−10.4865	13.49	13.69	2350^{+138}_{-125}
17	4337376700732832512	249.3277	−10.5117	14.31	14.56[a]	2537^{+222}_{-190}
18	4337372543204454144	249.3699	−10.5763	13.26	13.33	$307.5^{+4.5}_{-5.5}$
19	4337376288415957120	249.3703	−10.5152	14.91	15.21	4645^{+842}_{-628}
20	4337376528934134144	249.3904	−10.4833	14.79	14.90	2616^{+222}_{-190}
21	4337376460214656896	249.3975	−10.4786	14.50	14.75	2299^{+246}_{-204}
22	4337372985583902848	249.4100	−10.5507	15.17	15.44	4790^{+975}_{-709}
23	4337347598034360704	249.4194	−10.6498	13.39	13.51	$552.4^{+5.6}_{-6.4}$
24	4337372852442084096	249.4617	−10.5519	12.16	12.20	$202.7^{+1.3}_{-1.7}$
25	4337359452144088448	249.4686	−10.6339	13.39	13.42	$490.4^{+4.6}_{-5.4}$
26	4337371787290173952	249.5049	−10.5797	13.04	13.06	$581.7^{+13.3}_{-13.7}$
27	4337375218965869568	249.5108	−10.4688	12.90	12.95	$526.5^{+10.5}_{-10.5}$

Note.
[a] APASS photometry was not available. Pan-STARRS photometry is used with transformations from Jester et al. (2005).

identifier. Columns (3) and (4) provide the R.A. and decl. of the target, Column (5) gives the UCAC4 optical magnitude, and Column (6) gives the V-band magnitude from the AAVSO Photometric All-Sky Survey (APASS; Henden et al. 2016). Where APASS data were unavailable (targets #14, #15, and #17), we use Panoramic Survey Telescope and Rapid Response System (Pan-STARRS; Chambers et al. 2016) photometry in g′ and r′ and the transformations from Jester et al. (2005) for the V-band magnitude. Column (7) gives the Gaia distance from Bailer-Jones et al. (2018). Target distances appear bimodal (as seen in subsequent Figures 5 and 8) and fall into two distinct groups: a "near group" (14 stars) with distances ⩽600 pc and a "far group" (13 stars) with distances ⩾1000 pc.

2.1. APO Spectrophotometry

We obtained spectra of the 27 targets using the Apache Point Observatory (APO) Dual Imaging Spectrograph on 2019 May 2 and 3 (21 targets) and 2021 March 30 (six targets). The two channels of the spectrograph covered 4000–5240 Å with a reciprocal dispersion of 0.62 Å pixel^{-1} and 5720–6880 Å with a reciprocal dispersion of 0.58 Å pixel^{-1}, both using a 1200 line mm^{-1} grating. Observations were taken with 1″.5–2″ slits oriented at the parallactic angle. The seeing average was near 2″ over 1.3–1.7 air masses. Exposure times ranged from 300 to 600 s with one to two exposures per star. The continuum signal-to-noise ratio per pixel was in the range of 16–37 at 4500 Å and 40–71 at 6200 Å. The data were wavelength calibrated using HeNeAr exposures every 1–2 hr. Observations of spectrophotometric standard stars HZ 44, BD +33 2642, and BD +28 4211 from Oke (1990) over air masses 1.07–2.06 were used for flux calibration.

The spectra were processed in the standard manner with IRAF (Tody 1986) tasks to remove bias level using overscan regions on each exposure and correct for pixel-to-pixel variations with continuum flat fields. We corrected for atmospheric extinction over a range of air masses with standard-star data. The extinction-corrected standard stars differ from the Oke (1990) spectra by no more than 7% at the extreme blue end and by smaller percentages at the extreme red end. The calibrated APO spectra are available on Zenodo: https://doi.org/10.5281/zenodo.5639753.

2.2. WIRO Polarimetry

Polarimetric observations of the 27 stars were made on 2019 April 26–28, May 4, and June 6 using the OptiPol optical polarimeter (Jones et al. 2008) at the Cassegrain focus of the WIRO 2.3 m telescope. The instrument employs a Wollaston prism to image orthogonal polarizations simultaneously onto a 1024^2 Apogee Alta F16M with Kodak KAF-16803 CCD array

with 9 μm pixels at a scale of $0\rlap{.}''12$ pixel^{-1} (when on-chip 4×4 binning is used), yielding a $40'' \times 80''$ field of view. A sequence of exposures was obtained in the V-band filter for each target at four angular positions (0°, 22°.5, 45°, and 67°.5) of a half-wave plate. Exposure times ranged from 6 to 200 s, according to target brightness. Unpolarized standards BD +33 2642, BD +28 4211 (Schmidt et al. 1992), and HD 154892 (Turnshek et al. 1990) were observed to determine the instrumental polarization for each night.

The data from each position of the wave plate were processed in a standard manner using IRAF (Tody 1986) to remove contributions from dark current, bias level, and pixel-to-pixel sensitivity variations. We used the LACosmics Python script (based on algorithms from and developed by van Dokkum 2001) to clean cosmic rays from the data. We used a custom Python code to perform aperture photometry on each image and compute the normalized q and u Stokes parameters using the method from Tinbergen (2005).

Polarized standard stars HD 155197, HD 161056, and VI Cyg 12 (Schmidt et al. 1992) were used to determine an instrumental position angle offset of 81°.5 and verify the percent polarization. Average instrumental polarization was small ($q = -0.20$, $u = 0.19$). The instrumental polarization was subtracted in the q-u plane, and the calibrated Stokes parameters were calculated. Using these quantities, the percent polarization ($P_V{}'$) and the position angle east of north (P.A.) are given by the standard relations: $P_V{}' = \sqrt{q^2 + u^2}$ and P.A. $= \frac{1}{2}\tan^{-1}\frac{u}{q}$. To correct the data for positive bias, we used the relationship that $P_V = \sqrt{P_V{}'^2 - \sigma_P^2}$, where σ_P is the polarization uncertainty propagated from errors in q and u (Wardle & Kronberg 1974).

Table 2 reports the polarimetric results. Column (1) lists the target number corresponding to Table 1; Columns (2) and (3) list the q and u values; Column (4) lists the percent polarizations, P_V, and 1σ uncertainties; and Column (5) lists the position angles, P.A., and 1σ uncertainties.

Figure 1 shows the V-band polarization vectors overlaid on a $32' \times 18'$ version of the Spitzer field surrounding ζ Oph. The orientation of the numbered white vectors demonstrates the polarization position angle for each target in Table 1. The length of the vectors shows the percent polarization. The legend illustrates 1% polarization at PA = 0°. We also show the polarization of ζ Oph at V band to be 1.44% at PA = 126° (Serkowski et al. 1975).

A majority of the stars in Figure 1 show similar position angles and polarization percentages. The mean P.A. for the 27 targets is 103° with a standard deviation of 11°, and the mean P_V is 1.68% with a standard deviation of 0.46%. The mean position angle of the polarization vectors is smaller than that of ζ Oph, but the mean percent polarization is larger than that of ζ Oph (Serkowski et al. 1975). Targets at similar distances to ζ Oph, like #4 (224 pc) and #6 (252 pc), are in better agreement with the position angle of ζ Oph than targets at larger distances and have larger-than-average polarizations. Other stars at modest distances (278–500 pc; #11, #13, #14) and beyond exhibit a rotation in position angle relative to the nearest stars and have a notable uniformity in P_V and P.A.

To examine the polarization beyond ζ Oph, we subtracted the polarization of ζ Oph itself from each of our polarization measurements in the q-u plane. For ζ Oph, $q = -0.445$ and $u = -1.37$ from Serkowski et al. (1975). When added in

quadrature, the errors from our measurements dominate over the errors in the polarization of ζ Oph. Columns (6), (7), (8), and (9) of Table 2 provide the foreground-subtracted quantities, q_f, u_f, P_{Vf}, and P.A.$_f$.[1] Using the same notation as Figure 1, Figure 2 presents the foreground-subtracted polarization vectors on the infrared Spitzer image. This subtraction results in much smaller P_{Vf} for the three nearest stars (targets #4, #6, and #24) and an abrupt change in P.A. for the rest of the field. The foreground-subtracted mean values are $P_{Vf} = 1.29\%$ with a dispersion of 0.47% and P.A.$_f = 77°.2$ with a dispersion of 17°.8.

3. Analysis

3.1. Extinction Estimates

In order to investigate the interstellar extinction throughout the field of view, we estimated A_V using four different methods. Three of these methods, A_V(spectra), A_V(phot), and A_V(RJCE), assume $R_V = 3.1$ and are described in detail and compared below. The fourth, complementary but separate method allows R_V to deviate from the Milky Way average. The combination of these extinction estimates allows us to examine the dust properties as a function of distance.

3.1.1. Determining Target Spectral Types

As a prerequisite to calculating extinction, we first determined the spectral types of the target stars. We compared our continuum-normalized spectra to continuum-normalized PHOENIX stellar models (Husser et al. 2013) to determine approximate T_{eff} by visual examination. As another check on the spectral types, we used the spectral classification code PyHammer (Roulston et al. 2020). Visual inspection agreed with the PyHammer results within about 300 K.

While our optical spectra provide an estimate of the effective temperature for the target stars, their positions on the H-R diagram offer additional insight regarding their evolutionary status (i.e., log g). Figure 3 plots the absolute K magnitude (as computed from the distance modulus) versus T_{eff} for the near group (blue squares) and the far group (red squares). Cyan/magenta/black tracks show $10^{9.6}/10^{9}/10^{8}$ yr isochrones from Bressan et al. (2012, PARSEC, version 1.2S, adopting solar metallicity).[2] The main sequence emanates from the lower right corner of the plot. The main-sequence turnoffs are visible. The tracks change from points to encircled points as the stars evolve into giants (log g falls below 3). The near group of stars at distances $d < 600$ pc and z heights $\lesssim 240$ pc above the Galactic plane are consistent with near-main-sequence F–G V–IV stars (the track of small cyan points), for which we may reasonably adopt log $g = 4.0$ and metallicity [M/H] = 0, appropriate for the Galactic disk population. The far group of targets at distances $d > 1000$ pc and z heights > 400 pc are consistent with post-main-sequence giants with ages < 1 Gyr (the track of small magenta points as they transition into encircled points). At such young ages, the far group cannot—despite their larger z distances—be metal-poor thick-disk or halo stars. We adopt log $g = 3.0$ and metallicity [M/H] = 0 for these objects. For the two most luminous objects, #2 and #7, which are also among the most distant in our sample, we adopt log $g = 2.0$. We

---

[1] $q_f = q - (-0.445)$ and $u_f = u - (-1.37)$. P_{Vf} and P.A.$_f$ are constructed in the usual manner from these quantities.

[2] As computed using the web interface http://stev.oapd.inaf.it/cgi-bin/cmd on 2020 December 15.

Table 2
Polarization Data for the Target Stars in Table 1

Target	q (%)	u (%)	P_V (%)	P.A. (deg)	q_f (%)	u_f (%)	P_{Vf} (%)	P.A.$_f$ (deg)
ζ Oph	-0.45 ± 0.04	-1.37 ± 0.04	1.44 ± 0.04	126.0 ± 0.8	...	...	...	...
1	-1.04 ± 0.28	-0.36 ± 0.27	1.06 ± 0.28	99.5 ± 7.1	-0.60 ± 0.28	1.01 ± 0.27	1.14 ± 0.27	60.3 ± 6.8
2	-1.26 ± 0.23	-0.61 ± 0.25	1.38 ± 0.23	102.9 ± 5.0	-0.82 ± 0.23	0.76 ± 0.25	1.09 ± 0.24	68.5 ± 6.2
3	-1.78 ± 0.21	-1.00 ± 0.21	2.03 ± 0.21	104.7 ± 3.0	-1.34 ± 0.21	0.37 ± 0.21	1.37 ± 0.21	82.3 ± 4.3
4	-0.60 ± 0.10	-1.80 ± 0.10	1.89 ± 0.10	125.8 ± 1.5	-0.15 ± 0.10	-0.43 ± 0.10	0.45 ± 0.10	125.1 ± 6.3
5	-1.41 ± 0.18	-1.27 ± 0.18	1.89 ± 0.18	111.0 ± 2.7	-0.96 ± 0.18	0.10 ± 0.18	0.95 ± 0.18	87.0 ± 5.3
6	-0.81 ± 0.42	-1.82 ± 0.25	1.97 ± 0.29	123.0 ± 5.7	-0.37 ± 0.42	-0.45 ± 0.25	0.48 ± 0.33	115.5 ± 17.9
7	-1.68 ± 0.25	-0.97 ± 0.24	1.92 ± 0.25	105.0 ± 3.6	-1.23 ± 0.25	0.40 ± 0.24	1.27 ± 0.25	81.0 ± 5.3
8	-1.38 ± 0.29	-1.75 ± 0.28	2.21 ± 0.28	115.9 ± 3.7	-0.93 ± 0.29	-0.38 ± 0.28	0.97 ± 0.29	101.1 ± 8.0
9	-1.54 ± 0.16	-0.93 ± 0.16	1.79 ± 0.16	105.6 ± 2.6	-1.10 ± 0.16	0.44 ± 0.16	1.17 ± 0.16	79.1 ± 3.9
10	-1.93 ± 0.23	-1.08 ± 0.22	2.20 ± 0.23	104.6 ± 2.9	-1.48 ± 0.23	0.29 ± 0.22	1.50 ± 0.23	84.5 ± 4.2
11	-2.07 ± 0.35	-0.99 ± 0.35	2.27 ± 0.35	102.8 ± 4.4	-1.62 ± 0.35	0.38 ± 0.35	1.63 ± 0.35	83.4 ± 6.0
12	-1.05 ± 0.25	-1.89 ± 0.24	2.15 ± 0.24	120.5 ± 3.3	-0.60 ± 0.25	-0.52 ± 0.24	0.76 ± 0.25	110.3 ± 8.8
13	-1.03 ± 0.07	-0.85 ± 0.07	1.33 ± 0.07	109.8 ± 1.5	-0.58 ± 0.07	0.52 ± 0.07	0.78 ± 0.07	69.2 ± 2.6
14	-2.13 ± 0.42	-0.75 ± 0.42	2.22 ± 0.42	99.7 ± 5.3	-1.68 ± 0.42	0.62 ± 0.42	1.75 ± 0.42	79.9 ± 6.7
15	-1.55 ± 0.29	0.02 ± 0.31	1.52 ± 0.29	89.6 ± 5.7	-1.10 ± 0.29	1.39 ± 0.31	1.75 ± 0.30	64.2 ± 4.8
16	-1.75 ± 0.25	-0.89 ± 0.22	1.95 ± 0.24	103.5 ± 3.3	-1.30 ± 0.25	0.48 ± 0.22	1.37 ± 0.25	79.9 ± 4.6
17	-1.68 ± 0.24	-0.34 ± 0.23	1.70 ± 0.24	95.7 ± 3.9	-1.23 ± 0.24	1.03 ± 0.23	1.59 ± 0.24	70.1 ± 4.2
18	-1.39 ± 0.39	0.48 ± 0.39	1.42 ± 0.39	80.5 ± 7.6	-0.94 ± 0.39	1.85 ± 0.39	2.04 ± 0.39	58.5 ± 5.4
19	-1.63 ± 0.40	-0.72 ± 0.36	1.74 ± 0.39	101.9 ± 5.9	-1.18 ± 0.40	0.65 ± 0.36	1.29 ± 0.39	75.6 ± 7.8
20	-1.20 ± 0.29	-0.82 ± 0.28	1.42 ± 0.29	107.2 ± 5.6	-0.75 ± 0.29	0.55 ± 0.28	0.89 ± 0.29	72.0 ± 8.7
21	-1.33 ± 0.30	-0.23 ± 0.29	1.32 ± 0.30	94.9 ± 6.2	-0.88 ± 0.30	1.14 ± 0.29	1.41 ± 0.29	63.9 ± 5.9
22	-2.04 ± 0.40	0.66 ± 0.42	2.11 ± 0.40	81.0 ± 5.6	-1.60 ± 0.40	2.03 ± 0.42	2.55 ± 0.41	64.1 ± 4.5
23	-1.22 ± 0.15	-0.30 ± 0.15	1.25 ± 0.15	96.9 ± 3.4	-0.77 ± 0.15	1.07 ± 0.15	1.31 ± 0.15	63.0 ± 3.3
24	-0.78 ± 0.07	-0.75 ± 0.07	1.08 ± 0.07	111.9 ± 1.9	-0.34 ± 0.07	0.62 ± 0.07	0.70 ± 0.07	59.2 ± 2.9
25	-0.58 ± 0.53	-0.01 ± 0.46	0.24 ± 0.53	90.5 ± 22.7	-0.13 ± 0.53	1.36 ± 0.46	1.29 ± 0.46	47.8 ± 11.1
26	-1.89 ± 0.23	-0.15 ± 0.16	1.88 ± 0.23	92.3 ± 2.4	-1.44 ± 0.23	1.22 ± 0.16	1.88 ± 0.20	69.9 ± 2.9
27	-1.45 ± 0.12	-0.42 ± 0.12	1.50 ± 0.12	98.1 ± 2.3	-1.00 ± 0.12	0.95 ± 0.12	1.38 ± 0.12	68.3 ± 2.5

Note. f represents polarization values after subtracting ζ Oph in the q-u plane.

created similar plots with reduced-metallicity (-0.5 dex) isochrones for comparison and found that metallicity has negligible impact on the inferred ages and gravities.

Given these fundamental parameters ($T_{\rm eff}$, log g, [M/H]), we assigned a PHOENIX model spectrum to represent the intrinsic spectral energy distribution needed to characterize the interstellar extinction along each sight line. Table 3 lists target number in Column (1), adopted effective temperature in Column (2), adopted log g in Column (3), and corresponding approximate spectral type in Column (4). Our targets are F, G, and K stars that correspond to PHOENIX model temperatures in the range 5000–6100 K, based on the effective temperature versus spectral type sequence from Pecaut & Mamajek (2013). By visual comparison of PHOENIX models to spectra, we estimate that our classifications are accurate to ±300 K, or approximately three to four subtypes.

### 3.1.2. Fitting for A_V(spectra) with APO Spectra

As an initial extinction estimate, we calculated A_V using the APO spectra. We smoothed the stellar model templates and the data to 10 broad wavelength intervals, as only the overall shape of the spectrum is needed to fit for extinction. We normalized the stellar model from Table 3 and the flux-calibrated spectra at the longest wavelength interval, but the derived extinctions remain the same with any normalization. We then divided the spectra by the corresponding PHOENIX model to obtain a curve that reflects the wavelength-dependent interstellar extinction, A_λ. The curve was then fit using the Cardelli et al. (1989, Equations (1), (2), and (3)) optical reddening parameterization with a fixed $R_V = 3.1$ to obtain A_V(spectra). The

resulting range of A_V(spectra) is 0.79–3.27 mag, and values are tabulated in Column (5) of Table 3. Uncertainties on A_V(spectra) (also shown in Table 3, Column (5)) are dominated by uncertainty on the spectral type. We performed the same fitting process using stellar models 300 K below and above the chosen model and used the dispersion in the resultant values of A_V(spectra) as the 1σ uncertainties. The average uncertainty in A_V(spectra) is ≈ 0.3 mag.

3.1.3. Fitting for A_V(phot) with Publicly Available Photometry

Because our spectra cover only the optical range of the spectrum, we also estimated the extinction with photometry in the optical and IR. We performed the same extinction calculation with APASS photometric data in B, V, g' $r'i'z'y'$; Two Micron All Sky Survey (2MASS) JHK; and Spitzer 3.6 and 4.5 μm magnitudes as cataloged in the NASA/IPAC Infrared Science Archive (IRSA) database. APASS data are available for 24 of the 27 target stars (missing are #14, #15, and #17 on account of their proximity to ζ Oph). For those targets, we used photometric data from Pan-STARRS.

We normalized the stellar model from Table 3 to the photometry at 4.5 μm and then performed synthetic photometry on each model as described by Girardi et al. (2002) using published filter transmission curves specific to each bandpass. We divided the fluxes of the photometric measurements in each band by the synthetic stellar model fluxes and then fitted for A_V(phot) using the same approach as above, including the Cardelli et al. (1989) prescriptions for the optical and near-IR. Column (6) of Table 3 lists A_V(phot) derived from the photometric data. The resulting range of A_V(phot) is

Piccone & Kobulnicky
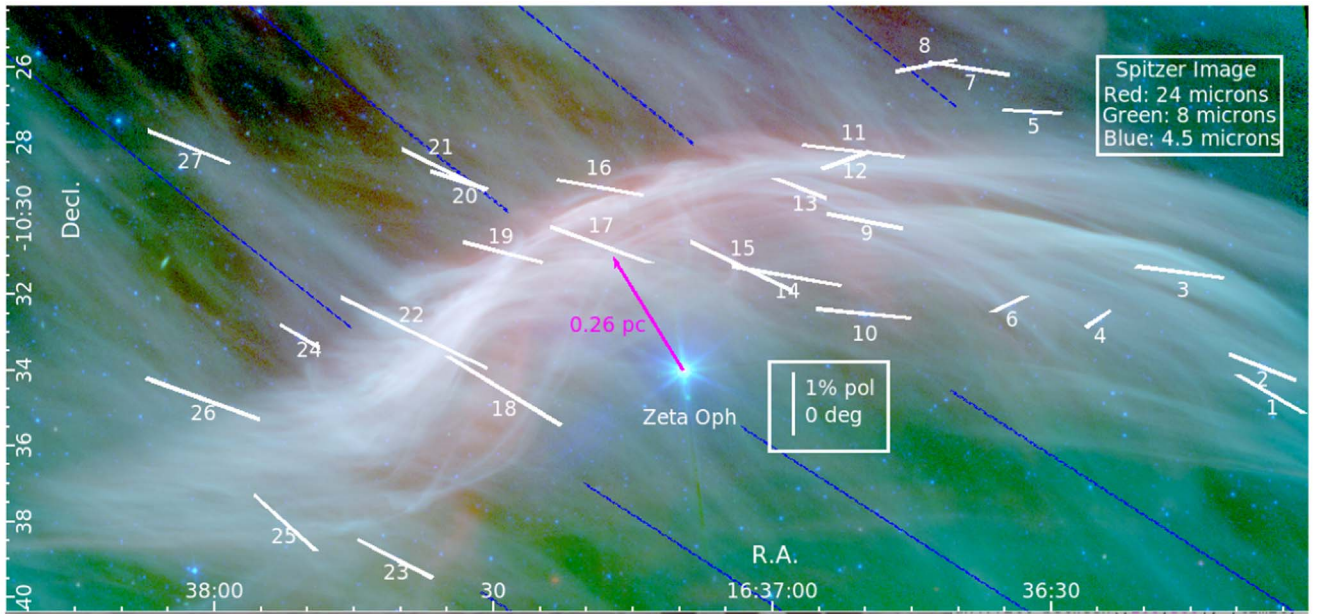
Figure 2. Foreground-subtracted polarization vectors, P_{Vf} and P.A.$_f$, overlaid on the same infrared images as in Figure 1. Blue dashed lines show the orientation of the 8 μm dust striations above and below the bow shock as traced by the Rolling Hough Transform from Clark et al. (2014), detailed in Section 3.3.

0.69–2.61 mag. Uncertainties again are dominated by uncertainties on the spectral type and are calculated in the same manner. The average error in A_V(phot) is $\approx$0.2 mag, somewhat smaller than that of the spectra on account of the larger wavelength range used.

Figure 4 shows an example of the technique used to estimate interstellar extinctions for target #1. The gray squares show the stellar model at each bandpass (F9, 6000 K, log g = 4.0) in AB magnitudes. The translucent blue circles show the reddened APO spectrum smoothed to 10 overall bins. Errors represent the standard deviation in each bin. The translucent red stars show the reddened photometry, which has errors directly from IRSA, APASS, and Pan-STARRS that are often too small to be visible in the figure. The spectrum and photometry differ slightly in AB mag prior to dereddening. This can be explained with an arbitrary grayshift resulting from clouds affecting the spectrophotometry during nonphotometric conditions. However, the shape of both the reddened spectra and photometry is always very similar, and that shape determines the reddening and extinction. The dark-blue circles show the spectrum after dereddening by A_V(spectra) = $1.35^{+0.25}_{-0.26}$ and R_V = 3.1, and the dark-red stars show the photometry after dereddening by A_V(phot) = $1.26^{+0.18}_{-0.20}$ and R_V = 3.1. The two estimates agree within their uncertainties and provide a good match to the model template.

3.1.4. Calculating A_V(RJCE) with the Rayleigh–Jeans Color Excess Method

The Rayleigh–Jeans color excess (RJCE) method (Majewski et al. 2011) also provides an estimation for A_V based on H-band and 4.5 μm photometry from 2MASS and Spitzer (Cutri et al. 2003; Fazio et al. 2004). The H−4.5 μm color is a robust measure of extinction regardless of temperature, metallicity, or surface gravity for the ubiquitous F–M stars that populate most Galactic fields. Using the relationships $A_K = 0.918(H−[4.5 \mu m]−0.08)$ and $A_V = 8.82A_K$ for $R_V = 3.1$, we determined A_V(RJCE) and uncertainties, as listed in Column (7) of Table 3.

A_V(RJCE) ranges from 0.55 to 2.54 mag with typical uncertainties $\approx$0.2 mag.

3.1.5. Comparisons between Extinction Estimates with R_V = 3.1.

To examine the validity of each A_V estimate, we compared the three values for each target in Figure 5. The left panel plots A_V(phot) versus A_V(spectra) in black circles and A_V(phot) versus A_V(RJCE) in blue squares. The line shows the 1:1 correspondence between the estimates. The black points show that A_V(spectra) and A_V(phot) are tightly correlated with a slope slightly less than unity. The strong correlation, with a Pearson correlation coefficient of 0.97, between A_V(spectra) and A_V(phot) affirms the consistency of these independent optically based measurements. The blue points show that A_V(phot) and A_V(RJCE) are correlated at small extinctions but then diverge, falling consistently above the 1:1 relation at higher extinctions. A_V(phot) and A_V(RJCE) are not well correlated, with a Pearson correlation coefficient of 0.57 for all target stars.

The right panel of Figure 5 shows A_V(phot) and A_V(RJCE) versus distance (lower x-axis) and distance above the plane (upper x-axis). Black points show A_V(phot), and blue points show A_V(RJCE). The green point designates ζ Oph (A_V = 1.02 mag, d = 182 pc), with its extinction arising within multiple foreground cloud complexes and an H II region (Wood et al. 2005; Choi et al. 2015). The dashed vertical line marks the scale height of dust in the Galactic plane, $z = 125^{+7}_{-7}$ pc (Marshall et al. 2006). In the near group of targets, A_V(RJCE) is similar to A_V(phot), with means of 1.27 ± 0.09 mag and 1.17 ± 0.08 mag, respectively (uncertainties represent the error of the mean). In the far group, A_V(RJCE) consistently falls below A_V(phot) with means of 1.70 ± 0.11 mag and 2.05 ± 0.09 mag, respectively. Figure 5 indicates that A_V(RJCE) is systematically less than A_V(phot) in the far group.

Regardless of measure used, it is clear that the extinction increases with distance. The far group has an average A_V(phot) 0.88 mag larger than the near group and an average A_V(RJCE) 0.43 mag larger than the near group. The Pearson correlation
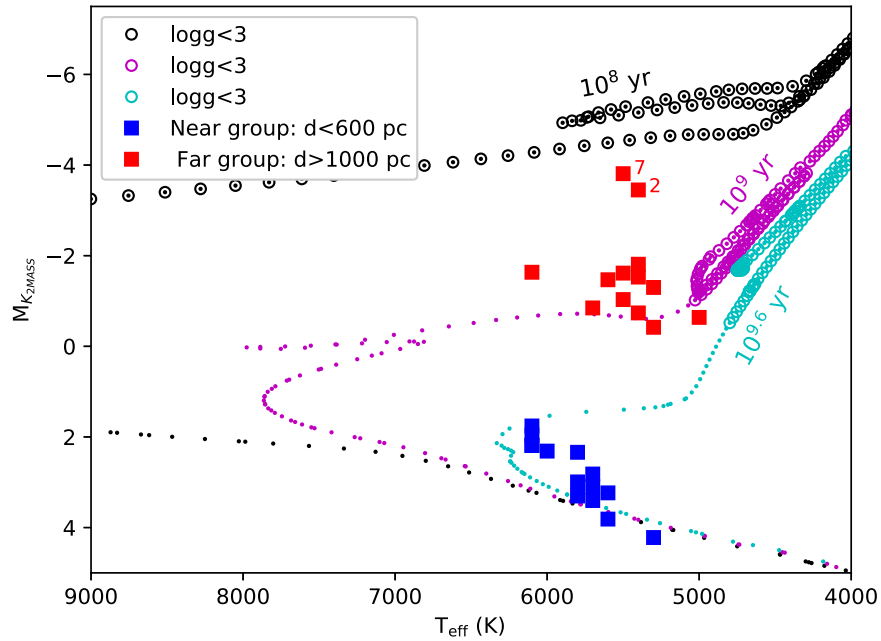
Figure 3. Absolute K magnitude vs. effective temperature for the near group of background stars (blue squares) and the far group (red squares). Colored tracks show solar-metallicity PARSEC (Bressan et al. 2012) isochrones at ages of $10^{9.6}/10^{9}/10^{8}$ yr, as labeled. Large symbols denote the approximate onset of giants at log $g < 3$. The near group is consistent with near-main-sequence F–G stars, while the far group consists of post-main-sequence giants.

coefficient between distance and A_V(phot) for all targets is 0.73, implying positive linear correlation. The correlation between distance and A_V(RJCE) is smaller: 0.5 for all targets. By examining the near and far group separately, we find that correlation in the far group is lower than in the near group for both A_V(phot) and A_V(RJCE). The difference between A_V(phot) and A_V(RJCE) in the far group suggests that the extinction depends on the wavelength range used for its calculation (visible vs. IR photometry), which indicates a departure from the average reddening curve in the Milky Way.

3.1.6. Determining E(B − V) and Incrementally Dereddening along the Line of Sight

The discrepancy between extinction estimates (primarily in the far group) motivates a technique to explore the properties of the different dust populations with distance. We therefore developed a tool to perform Incremental DeReddening Along the Line of Sight (IDEALS), allowing us to investigate both A_V and R_V as a function of distance.

Following Fitzpatrick et al. (2019), we constructed the extinction curve for the targets over optical and infrared wavelengths. Using the B, V, and $g' r'i'z'y'$ magnitudes from the APASS database (or Pan-STARRS when required) and the 2MASS JHK and Spitzer 3.6 and 4.5 μm magnitudes, we normalized the stellar model from Table 3 and photometry at V band and performed synthetic photometry on each model as described for A_V(phot). For comparison to the previous estimates, we assumed the Fitzpatrick et al. (2019) empirical extinction curves and fit for the best A_V; however, we also allowed R_V to vary. We directly calculated the color excess, $E(\lambda - V)$, at each bandpass relative to V band in order to encompass both A_V and R_V into one measure. Column (7) of Table 3 lists $E(B - V)$ for each target. We then expressed the reddening relative to V band in the standard nomenclature from

Johnson (1965),

$$k(\lambda - V) = \frac{E(\lambda - V)}{E(B - V)}. \quad (1)$$

Figure 6 plots $k(\lambda - V)$, the extinction curve, versus inverse wavelength. Black lines show the extinction curves from Fitzpatrick et al. (2019).[3] Line styles denote different R_V, with larger R_V creating a steeper slope in $k(\lambda - V)$. Labels along the bottom mark standard bandpasses at their corresponding inverse wavelength. Blue and red points denote average values of $k(\lambda - V)$ for the near and far groups, respectively. Error bars represent the error of the mean within each band. Any systematic errors on our adopted stellar T_{eff} would merely shift the points up or down together relative to the reddening curves. While they are similar in the optical, the near group of targets (blue) follows a smaller R_V trend than the far group (red) in the infrared. However, both groups are close to the Milky Way average of $R_V = 3.1$, shown by the solid black line.

The green circles in Figure 6 show the extinction curve of ζ Oph. Owing to its brightness, there are no measurements of ζ Oph on a modern photometric system. Accordingly, we adopted optical $BVRI$ magnitudes from Johnson (1965) and used the equations of Jester et al. (2005) and Fernie (1983) to transform these into $g'r'i'z'$ magnitudes. In the infrared we used the 2MASS JHK and Spitzer 3.6 and 4.5 μm fluxes from IRSA and employed the corresponding zero-points to obtain magnitudes. At 3.6 and 4.5 μm the Spitzer fluxes are $\sim$30% smaller than the ground-based measurements of Gehrz et al. (1974), so we adopted the average of the two fluxes. For the intrinsic spectral energy distribution we selected the $T_{eff} = 31,000$ K, log $g = 4.5$ "BT-settl" model atmosphere of Allard et al. (2011), which yields very similar results to the older Castelli & Kurucz (2003) models. Despite larger uncertainties resulting from the photometric transformations, the reddening curve for ζ Oph is consistent with mean

---

3 These closely match the Cardelli et al. (1989) analytic extinction curves.

Table 3
Spectral Types and Extinction Values for the Target Stars in Table 1

Target	$T_{\rm eff}$ (K)	log g	Sp. Type	A_V (mag) Assuming $R_V = 3.1$			$E(B-V)$ (mag)
				A_V(spectra)	A_V(phot)	A_V(RJCE)	
1	6000	4.00	F9	$1.35^{+0.25}_{-0.26}$	$1.26^{+0.18}_{-0.20}$	1.43 ± 0.20	$0.49^{+0.08}_{-0.08}$
2	5400	2.50	G9	$3.27^{+0.33}_{-0.35}$	$2.61^{+0.23}_{-0.25}$	1.72 ± 0.20	$1.07^{+0.11}_{-0.11}$
3	5600	3.00	G6	$2.33^{+0.28}_{-0.31}$	$1.99^{+0.21}_{-0.24}$	1.52 ± 0.20	$0.78^{+0.09}_{-0.10}$
4	5700	4.00	G3	$1.01^{+0.26}_{-0.29}$	$0.81^{+0.20}_{-0.23}$	0.91 ± 0.20	$0.35^{+0.08}_{-0.09}$
5	5800	4.00	G2	$1.70^{+0.25}_{-0.28}$	$1.44^{+0.19}_{-0.22}$	1.28 ± 0.20	$0.56^{+0.08}_{-0.09}$
6	5600	4.00	G6	$1.23^{+0.26}_{-0.30}$	$0.99^{+0.21}_{-0.24}$	1.17 ± 0.20	$0.48^{+0.09}_{-0.10}$
7	5500	2.50	G8	$2.72^{+0.29}_{-0.36}$	$2.5^{+0.22}_{-0.25}$	2.23 ± 0.20	$0.88^{+0.09}_{-0.12}$
8	5300	3.00	K0	$2.90^{+0.32}_{-0.33}$	$2.28^{+0.24}_{-0.27}$	1.82 ± 0.20	$0.90^{+0.10}_{-0.10}$
9	5700	4.00	G3	$1.29^{+0.26}_{-0.29}$	$1.19^{+0.20}_{-0.23}$	1.20 ± 0.20	$0.43^{+0.08}_{-0.09}$
10	5400	3.00	G9	$2.86^{+0.29}_{-0.34}$	$2.36^{+0.22}_{-0.26}$	1.70 ± 0.20	$0.87^{+0.09}_{-0.11}$
11	5300	4.00	K0	$2.40^{+0.30}_{-0.32}$	$1.73^{+0.24}_{-0.27}$	1.83 ± 0.20	$0.66^{+0.10}_{-0.09}$
12	5700	3.00	G3	$2.56^{+0.29}_{-0.29}$	$2.24^{+0.21}_{-0.22}$	1.78 ± 0.20	$0.77^{+0.10}_{-0.09}$
13	6100	4.00	F9	$1.30^{+0.25}_{-0.25}$	$1.21^{+0.18}_{-0.19}$	1.66 ± 0.20	$0.40^{+0.08}_{-0.08}$
14[a]	5800	4.00	G3	$2.07^{+0.25}_{-0.28}$	$1.54^{+0.19}_{-0.22}$	1.52 ± 0.20	$0.63^{+0.08}_{-0.09}$
15[a]	5300	3.00	K0	$2.30^{+0.32}_{-0.33}$	$1.71^{+0.24}_{-0.27}$	1.85 ± 0.20	$0.69^{+0.10}_{-0.10}$
16	5500	3.00	G8	$2.05^{+0.29}_{-0.32}$	$1.83^{+0.22}_{-0.24}$	1.81 ± 0.20	$0.52^{+0.10}_{-0.10}$
17[a]	5500	3.00	G8	$2.31^{+0.29}_{-0.32}$	$1.90^{+0.22}_{-0.24}$	1.09 ± 0.20	$0.65^{+0.10}_{-0.10}$
18	5600	4.00	G6	$1.39^{+0.27}_{-0.30}$	$1.09^{+0.21}_{-0.24}$	1.39 ± 0.20	$0.39^{+0.09}_{-0.10}$
19	6100	3.00	F9	$2.70^{+0.26}_{-0.27}$	$2.22^{+0.18}_{-0.20}$	1.12 ± 0.20	$0.72^{+0.08}_{-0.09}$
20	5000	3.00	K2	$1.42^{+0.33}_{-0.39}$	$1.41^{+0.27}_{-0.32}$	2.54 ± 0.20	$0.39^{+0.10}_{-0.12}$
21	5400	3.00	G9	$2.38^{+0.28}_{-0.34}$	$1.92^{+0.22}_{-0.26}$	1.38 ± 0.20	$0.62^{+0.09}_{-0.11}$
22	5400	3.00	G9	$2.77^{+0.29}_{-0.34}$	$1.95^{+0.22}_{-0.26}$	1.60 ± 0.20	$0.59^{+0.09}_{-0.11}$
23	6100	4.00	F9	$1.64^{+0.24}_{-0.25}$	$1.37^{+0.18}_{-0.19}$	1.26 ± 0.20	$0.56^{+0.08}_{-0.08}$
24	5700	4.00	G3	$0.79^{+0.26}_{-0.29}$	$0.69^{+0.20}_{-0.23}$	0.55 ± 0.20	$0.30^{+0.08}_{-0.09}$
25	5800	4.00	G3	$1.14^{+0.25}_{-0.28}$	$1.16^{+0.19}_{-0.22}$	1.15 ± 0.20	$0.42^{+0.08}_{-0.09}$
26	6100	4.00	F9	$0.96^{+0.25}_{-0.25}$	$1.04^{+0.18}_{-0.19}$	1.38 ± 0.20	$0.35^{+0.08}_{-0.08}$
27	6100	4.00	F9	$0.84^{+0.25}_{-0.25}$	$0.87^{+0.18}_{-0.19}$	0.99 ± 0.20	$0.31^{+0.08}_{-0.08}$

Note.
[a] APASS photometry was not available. Pan-STARRS photometry was used instead with transformations from Jester et al. (2005).

interstellar $R_V = 3.1$ dust, indicating that the dust in the $d < 182$ pc foreground is "average."

To examine R_V with distance, we constructed reddening curves for the near and far groups with their average foreground reddening removed. This is the crux of the IDEALS technique: it can explore dust properties at different distances along a line of sight by incrementally removing a well-determined foreground. Cyan stars in Figure 6 show the near group with the reddening of ζ Oph subtracted. With the foreground (ζ Oph) removed, the near group follows a smaller mean $R_V \approx 2.4$. Magenta stars show the far group with the average reddening of the near group subtracted. After subtracting the average of the near group, the far group has a noticeably greater mean $R_V \approx 3.6$.

3.2. A Highly Polarizing Dust Component

Observations of 180 sight lines from Serkowski et al. (1975) indicate that while polarization and color excess are not correlated, there is a maximum amount of polarization per unit reddening of $P_V = 9.1E(B - V)$. In their sample, only rarely do stars fall above this limit. More recent measurements (e.g., Andersson et al. 2015) continue to support this observational upper limit. Figure 7 plots P_{Vf} versus $E(B - V)_f$ (the foreground-subtracted color excess, adopting $E(B - V) = 0.33$ mag for ζ Oph) for the near group to examine the polarization efficiency of dust between ζ Oph and the stars in the immediate

background. The dashed line shows the observational limit proposed by Serkowski et al. (1975), and the shaded region denotes the "permitted" region below this limit. The foreground-subtracted polarizations (labeled by target number) in the near group are high, often above the limit. This suggests that the near group of stars lies behind or is embedded within a population of dust grains more efficiently polarizing than the typical ISM.

The negative color excess of target #24, along with its close distance ($d = 203$ pc), may indicate that it lies in the foreground of ζ Oph, which is entirely possible when taking into account the uncertainties in the Gaia distance of ζ Oph. To analyze this possibility, we replicated Figure 7 with the color excess and polarization of target #24 as the values for foreground subtraction. Target #24 has an $E(B - V) = 0.30^{+0.08}_{-0.09}$ and a raw polarization of $P_V = 1.09\% \pm 0.07\%$ at $111°9 \pm 1°82$. Although the group of targets in Figure 7 shifts slightly to the right, the figure and foreground-subtracted polarizations and color excesses remain essentially the same despite the choice of foreground reference star.

3.3. The Bow Shock and Striation Dust Structures

While the bow shock is certainly in close proximity to and associated with ζ Oph, the location and properties of the infrared striations present in Figures 1 and 2 are less clear. Both the bow shock and striations appear in all three wavelengths of
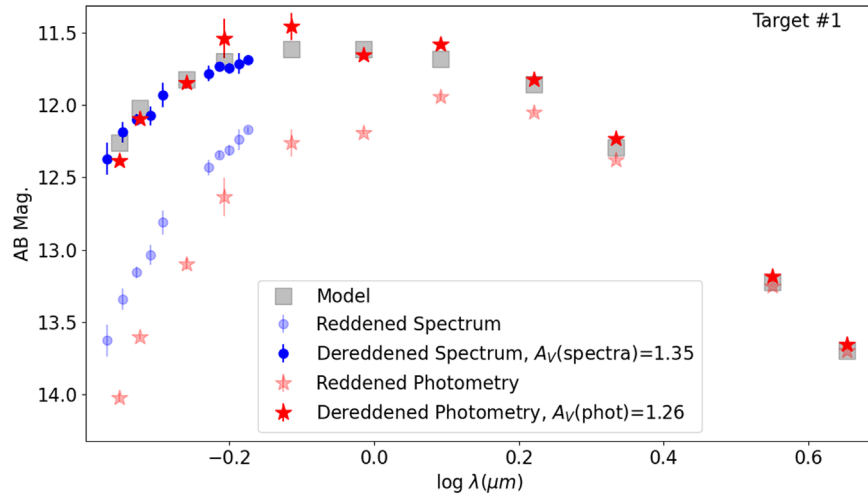
Figure 4. Reddening correction and extinction estimation for target #1. The gray squares show the smoothed stellar model (6000 K, $\log g = 4.0$) corresponding to the F9 spectral type. Circles show the reddened APO spectrum (light blue) and APO spectrum after dereddening by A_V(spectra) $= 1.35^{+0.25}_{-0.26}$ and $R_V = 3.1$ (dark blue). Stars show the reddened photometry (light red) and photometry after dereddening by A_V(phot) $= 1.26^{+0.18}_{-0.20}$ and $R_V = 3.1$ (dark red).

the Spitzer images, but most strongly at $8\,\mu$m, a wavelength dominated by polycyclic aromatic hydrocarbons (PAHs) that are excited by the UV radiation from hot stars. The clear signature of PAH emission from the striations demands illumination by UV photons, circumstantially placing them in close proximity to ζ Oph. As an O9.2IV star ($T_{\rm eff} = 31{,}000$ K, $R_\star = 7.2\,R_\odot$), ζ Oph dominates the radiant energy in its vicinity. From the catalog of Galactic OB stars (Reed 2003), we find no other O or early B stars within 50 pc of ζ Oph. At a distance of $z \sim 74$ pc above the Galactic plane, ζ Oph is the leading candidate for the source of far-UV photons exciting the PAH molecules (Tielens 2008) in the striations. The ratio of specific intensities at 8 and $24\,\mu$m, I_8/I_{24}, is ≈ 0.14 for the bow shock (redder in Figure 2) and ≈ 0.20 for the striations (greener in Figure 2), suggesting a larger PAH contribution in the latter. Likewise, the $8\,\mu$m/$4.5\,\mu$m (a band free of PAH contributions) ratio increases from ≈ 8.5 in the bow shock to ≈ 20 in the striations. This is similar to the value observed in established high-PAH photon-dominated regions (Churchwell et al. 2006; Deharveng et al. 2009). The disparate colors between the bow shock and striations indicate two distinct dust structures having a different set of physical conditions and possibly different grain properties.

To quantify the orientation of the dust striations and compare them to the polarization position angles in this field, we employed the Rolling Hough Transform from Clark et al. (2014). Their code reads images and calculates $R(\theta, x, y)$, a function that encodes intensity as a function of angle, θ, for components in the image at locations x and y. We performed this process using regions of the $8\,\mu$m Spitzer image lying directly above and below the prominent bow shock structure, excluding the bow shock because of its high intensity and dominance over the diffuse striations. By integrating $R(\theta, x, y)$ for each x and y with Equations (7) and (8) from Clark et al. (2014), we obtained the overall orientation angles for the striated regions directly above and below the bow shock. In Figure 2, the blue dashed lines show the average orientation of the striations above and below the bow shock, $51\overset{\circ}{.}6$ and $57\overset{\circ}{.}2$, respectively.

4. Discussion

The extinction and polarization data provide a clear picture of the dust along these lines of sight. While the foreground dust masks most of the variation in the form of the extinction curve, removal of that component reveals the interesting structures beyond.

4.1. Dust Populations along the Line of Sight

The correlation between A_V(RJCE) and A_V(phot) decreases at greater extinctions and distances. This is clearly demonstrated in Figure 5 and in the correlation coefficients calculated in Section 3.1.5. This indicates—most dramatically at larger extinctions—a departure of the reddening curve from the Milky Way average, the shape of which is assumed in the three methods used in Figure 5. We conclude from Figure 5 that the reddening curve for the high-extinction, far group differs from that of the low-extinction, near group.

The $k(\lambda - V)$ trends in Figure 6 suggest that the near group of stars is reddened by a population of dust with $R_V \approx 2.4$, while the far group is reddened by a population of dust with $R_V \approx 3.6$. The small R_V in the near group indicates an excess of small grains (as discussed in Section 1) just behind ζ Oph in a "mid-distance cloud." An excess of large grains (or deficit of small grains) above the Galactic plane, located in a "distant cloud," could plausibly explain the high R_V in the far group. On its own, the far group shows minimal correlation between extinction and distance (Pearson correlation coefficient of 0.47 for A_V(phot) and 0.21 for A_V(RJCE)) in Figure 5. This indicates that the additional extinction affecting the far group lies in the 600–2000 pc gap separating the two groups, thereby extincting the far group somewhat uniformly, although the dispersion of extinctions suggests some patchiness in dust coverage. Of course, both of these dust components idealized as discrete slabs may actually consist of smaller constituent clouds.

Figure 8 illustrates the preferred configuration of dust along the line of sight. The top panel shows P_{Vf} versus distance. The second panel shows $E(B - V)_f$, the foreground-subtracted color excess. The two bottom panels show A_{Vf} and R_{Vf}, which were obtained by dereddening using the foreground parameters of
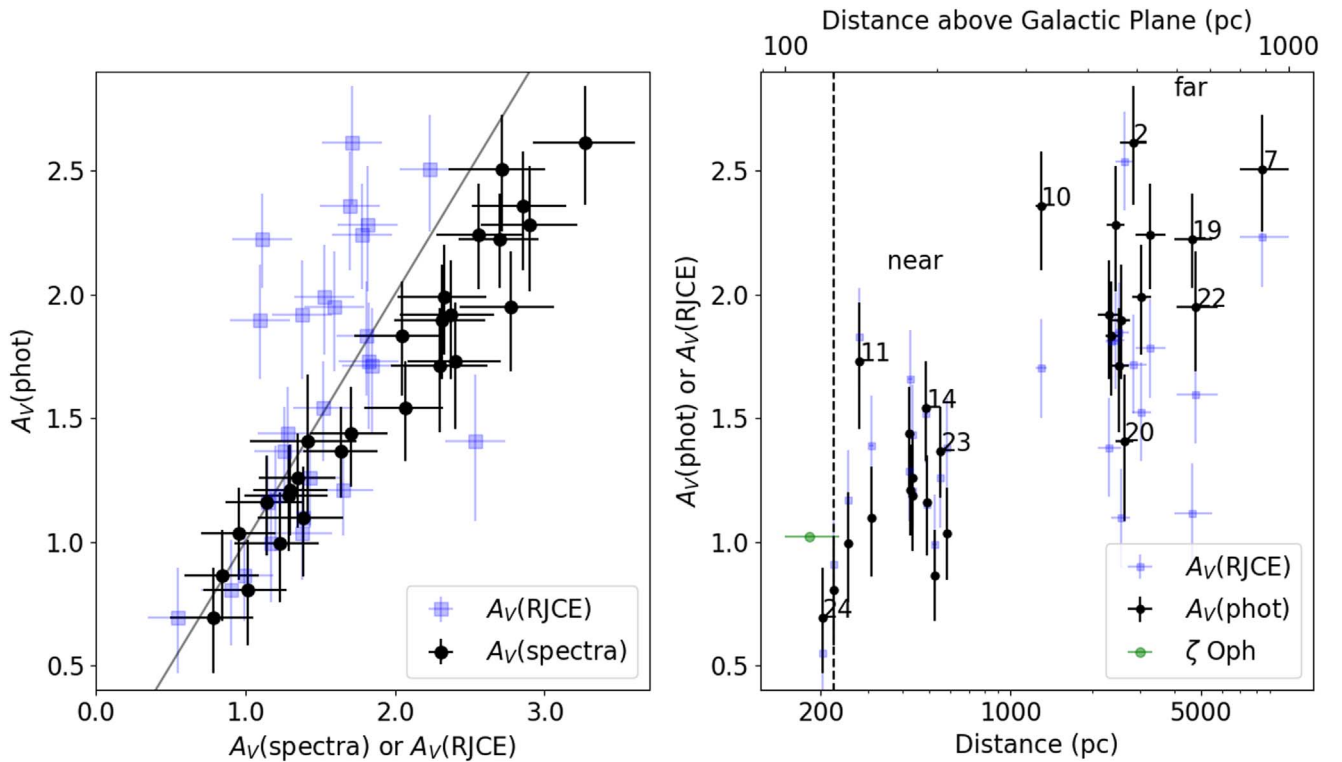
Figure 5. Left: A_V(phot) vs. A_V(spectra) in black circles and A_V(phot) vs. A_V(RJCE) in blue squares. The solid line shows what would be a 1:1 correspondence between estimates. Right: A_V(phot) in black and A_V(RJCE) in blue vs. distance and distance above the Galactic plane. Some target numbers are shown for clarity. The green point marks ζ Oph, and the near and far groups are labeled. A_V(RJCE) is consistently smaller than A_V(phot) at large extinctions and distances.

ζ Oph[4] and refitting the Fitzpatrick et al. (2019) extinction curve. Shaded gray regions represent the proposed two discrete dust populations that lie in the background of ζ Oph: a highly polarizing mid-distance 200–300 pc component and a non-polarizing 600–2000 pc distant component.

In the top panel, P_{Vf} increases sharply just beyond targets #4, #6, and #24 (203–252 pc) from 0.5% to as high as 2%. The substantial increase in polarization occurs in the same dust that creates only a small increase in color excess ($\Delta E(B - V) \approx 0.08$, visible in the second panel). This suggests a mid-distance dust component with high grain alignment efficiency somewhere in the vicinity of 200–300 pc. These sight lines raise the interesting possibility that the bulk of interstellar polarization may take place within a very small volume fraction of the ISM if such highly polarizing dust structures are common. The polarization then levels off below 2% at large distances. Although there is some dispersion in the far group, the polarization is consistently between 1% and 2%.

As distance increases, $E(B - V)_f$ also increases for the first few targets and then flattens for the remainder of the near group. The dispersion in $E(B - V)_f$ becomes greater at larger distances, and the mean $E(B - V)_f$ is larger than in the near group. A_{Vf} reflects the same trends as $E(B - V)_f$, increasing consistently with distance. Because $E(B - V)_f$ and A_{Vf} increase with distance but P_{Vf} does not, we conclude that the distant dust population (located between 600 and 2000 pc) extincts background light but does not create a noticeable polarization signature. This lack of polarization signature at large distances may stem from a tangled magnetic field, a weak or absent magnetic field, or a magnetic field oriented along the line of

sight. We are not able to distinguish which of these scenarios is at work, so we simply refer to this dust component as nonpolarizing.

The bottom panel shows R_{Vf}, the best fit for R_V after dereddening by the foreground of ζ Oph. For the targets with the lowest A_{Vf} and nearest distances (#4 and #6), fits of R_{Vf} are unreliable because there is very little reddening to fit, so R_{Vf} is set arbitrarily to zero. The R_{Vf} of the near group is low (1.8 ± 0.7), matching the $R_V \approx 2.4$ obtained for the foreground-subtracted near group in Figure 6. R_{Vf} increases with distance toward the far group to 2.6 ± 0.4. After further dereddening by the average extinction of the near group, the far group shifts toward a larger $R_V = 3.1 \pm 1.0$ (matching the $R_V \approx 3.6$ obtained in Figure 6).

While an average R_V for the Milky Way is established, it is based on O-, B-, and A-type stars near the midplane and does not account for possible variations throughout the Galaxy (Schultz & Wiemer 1975; Sneden et al. 1978). R_V is known to vary from values near 2 (Larson et al. 2000) to more than 6 (Johnson 1965). Whittet (1977) discovered variations with Galactic longitude that suggest changes in the size distribution of dust grains in the local spiral arm. Dust at high Galactic latitudes is known to be inconsistent with standard reddening laws, and no single R_V can explain observations of both the optical and ultraviolet extinctions toward extragalactic sources (Peek & Schiminovich 2013). It is fair to assume that dust properties vary throughout the Milky Way, possibly changing significantly along sight lines outside of the Galactic plane like ζ Oph ($b = 24°$). HD 210121 (B7II) lies below the Galactic plane and is also obscured by a diffuse cloud. The sight line toward that star has a low $R_V \approx 2.1$ (Larson et al. 2000), demonstrating that the smaller-than-average R_V in the near

---

4   $E(B - V) = 0.33$ from Ducati (2002) and Pecaut & Mamajek (2013).
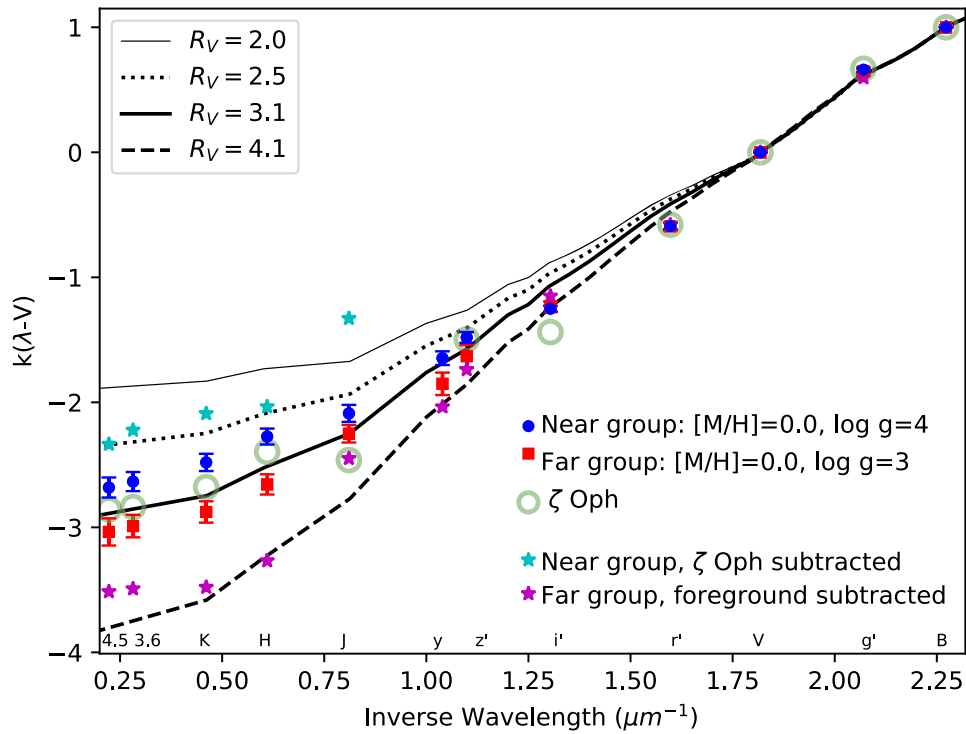
Figure 6. Extinction curves represented by the reddening relative to V band, i.e., $E(\lambda - V)$ per $E(B - V)$ vs. inverse wavelength in microns. Blue points mark the mean and error of the mean for the near group of 14 stars, red points mark the mean of the far group of 13 stars, cyan stars are the mean of the near group with the reddening of ζ Oph subtracted, and magenta stars are the mean of the far group with the reddening of the near group subtracted. Green circles represent ζ Oph. Tracks denote the canonical Milky Way reddening curves from Fitzpatrick et al. (2019) for a range of $R_V = 2.0/2.5/3.1/4.1$, according to the legend.
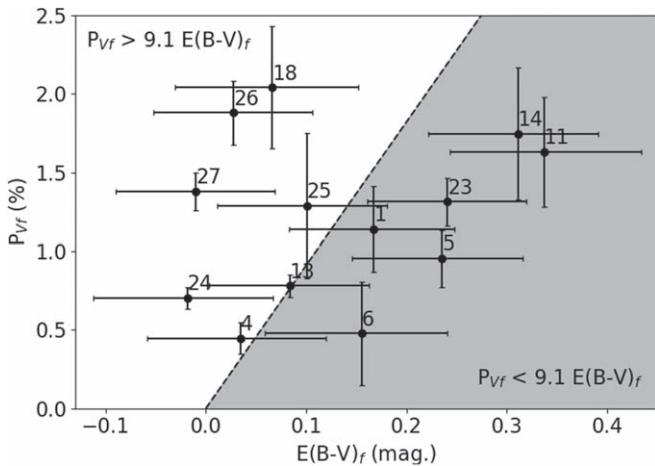
Figure 7. Percent polarization vs. color excess with the foreground of ζ Oph removed from each. The dashed line shows the observed maximum polarization per unit reddening of dust, $P_V = 9.1E(B - V)$ (Serkowski et al. 1975). Many targets in the nearby group fall above the line and are therefore highly polarized for the amount of reddening.

group may be a more global trend for diffuse clouds like those toward ζ Oph. In fact, many high-latitude clouds have enhanced abundances of relatively small dust grains (Larson & Whittet 2005).

### 4.2. Magnetic Field Characteristics and Relation to Dust Structures

Figure 7 indicates that the mid-distance dust directly behind ζ Oph is highly polarizing. It is likely that the high polarization per reddening arises from dust behind ζ Oph, as that star itself

falls far below the Serkowski limit, with $E(B - V) = 0.33$ and $P_V = 1.44\%$ (Serkowski et al. 1975). This highly polarizing component is not entirely novel, as Gontcharov & Mosenkov (2019) found sources in an all-sky polarization survey with $P_V > 9.1 E(B - V)$. They explain that this may be the result of an underestimate in $E(B - V)$, a nonstandard reddening law, or simply a violation of the observational upper limit. In our case, the nearby group of stars has an $E(B - V)_f$ that is well constrained. The high $P_V/E(B - V)$ ratio, which is substantially in excess of the limit from Serkowski et al. (1975), may then be the result of the nonstandard reddening law seen in the near group or dust that is more efficiently polarized than typical ISM material.

The polarization vectors in Figure 2 show the direction of the projected magnetic field with an average P.A. $= 77°$ and a dispersion of $18°$. The Rolling Hough Transform provides an average direction for the striations below and above the bow shock (blue dashed lines in Figure 2) of $57°.2$ and $51°.6$, respectively. This indicates that the polarization vectors are aligned with the infrared dust striations in the field of view. Taken together, the infrared images, polarization data, and striation orientation reveal a striated (P.A. $\approx 55°$) PAH-emitting cloud spanning the field of view in close proximity to ζ Oph that hosts the aligned grains that polarize background starlight at a similar position angle.

The main arc of the bow shock is approximately perpendicular to the projected magnetic field, while the proper motion of ζ Oph is parallel. The magnetic field does not appear to follow the filaments in the bow shock, nor is there any apparent deviation in P.A. even near the highest surface brightness portions of the nebula. The location and morphology of the bow shock are likely a result of the motion of ζ Oph and do not depend on the magnetic field orientation. Evidently, the bow
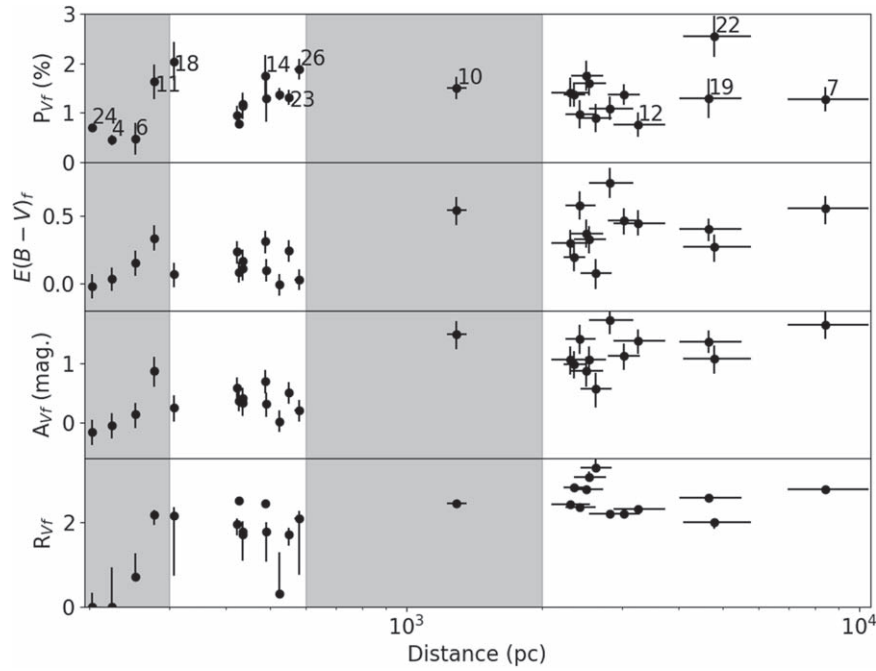
Figure 8. P_{Vf}, $E(B-V)_f$, A_{Vf}, and R_{Vf} with distance. Gray regions represent likely locations of dust along the line of sight, the highly polarizing mid-distance dust, and the nonpolarizing dust at a greater distance. Only some target numbers are shown for clarity.

shock contributes negligibly to the polarization, while the background striated medium is the strongly polarizing agent.

4.3. An Optically Thin Bow Shock Nebula

A brief examination of specific targets shows that there are small-scale angular variations across the field of view, as well as variations along adjacent lines of sight. For example, target #22 has a significantly larger P_{Vf} than target #19 (2.56% vs. 1.25%), despite the smaller $E(B-V)_f$ (0.27 vs. 0.40), similar location (within $\approx 2'$), similar P.A.$_f$ (64° vs. 76°), and almost identical distance (4790 pc vs. 4645 pc). Targets #11 and #12 lie within 30″ of each other, but at very different distances (278 and 3246 pc, respectively). Target #12 is understandably more reddened at a large distance but has a smaller P_{Vf} (0.45% vs. 1.60% for #11) and very different PA$_f$ (110° vs. 83° for #11) than surrounding targets. The areal density of background sources is not sufficient to probe small-scale dust variations in a rigorous manner, but the variations on small angular scales and with distance are clear.

We have not sampled enough targets to determine whether the bow shock nebula affects extinction. We find no clear difference in extinction between targets located directly behind (on) the bow shock and those off the bow shock. It is likely that distance is the primary parameter driving extinction, as seen in Figure 8. However, given that the optical depth of the bow shock at optical and UV wavelengths is expected to be small, it is not surprising that the prominent infrared nebula does not produce an obvious signature of increased extinction. The median ratio of nebular far-infrared luminosity to stellar luminosity is $L_{IR}/L_* \approx 0.003$ in bow shock nebulae (<0.001 in the case of ζ Oph), indicating that only a small fraction of the stellar energy is intercepted and reradiated by the dust in the nebula (Kobulnicky et al. 2017). The vast majority of infrared bow shock nebulae are optically thin, at least globally, a conclusion echoed by Henney & Arthur (2019). This does not rule out the possible existence of optically thick clumps on

small scales, but it does constrain them to have a small covering factor. The probability that one of the observed sight lines toward background stars would intercept such a clump is small, so the lack of an unambiguous signature in the extinction or polarization of background targets is unsurprising.

5. Summary

Using optical polarimetry and spectrophotometry, we have examined the polarization and reddening along the lines of sight to the 27 background stars surrounding the O9.2IV star ζ Oph. We have developed a technique to incrementally subtract foreground reddening and polarization. This has allowed us to characterize the dust along the line of sight to the target stars, probing differences that would otherwise be masked by a sight-line average.

1. The dust characteristics along the sight lines surrounding ζ Oph vary with distance and can be represented as three distinct populations: the foreground dust ($R_V \approx 3.1$), the highly polarizing mid-distance dust ($R_V < 3.1$), and the nonpolarizing distant dust ($R_V > 3.1$). The superposition of different dust populations along the line of sight leads to a sight-line-averaged R_V that is close to typical for the ISM, masking pronounced variations in the reddening curve with distance.

2. After subtracting the foreground characterized by the polarization of ζ Oph, the position angles become approximately parallel to the PAH-emitting infrared striations. The polarization most likely arises from the mid-distance dust responsible for those striations. We conclude that the dust is located behind—but in close proximity to—ζ Oph and is illuminated by the star's UV irradiation. With the foreground $R_V = 3.1$ dust removed, the mid-distance dust has an $R_V \approx 2.4$, suggesting an overabundance of small dust grains. This mid-distance dust (200–300 pc) is highly polarizing. It has a

polarization efficiency larger than the limit observed by Serkowski et al. (1975; $P_V/E(B - V) > 9.1$). The high $P_{Vf}/E(B - V)_f$ toward a number of stars over a limited path length (≈ 200 pc) indicates that large changes in polarization can occur over small increments in dust column density. This suggests that a very small fractional ISM volume containing populations of unusually small, highly aligned grains may dominate the interstellar polarization signature.

3. The distant dust (600–2000 pc) does not create a distinct polarization signature and has $R_V \approx 3.6$. The lack of polarization may stem from many factors, like a nonexistent or tangled magnetic field or a magnetic field oriented along the line of sight. The larger-than-average R_V implies an excess of large dust grains at large distances above the Galactic plane ($z > 250$ pc). In the simplest case, this may hold true for the entire Milky Way above the Galactic plane.

A complete understanding of variations in dust properties is essential in correcting for extinction and motivates further investigation into R_V above the Galactic plane to obtain a clear picture of dust properties throughout the Galaxy. The reddening map from Green et al. (2019) is dependent on R_V, and they emphasize that extinction maps derived from their reddenings without knowledge of the spatial dependence of R_V will introduce large-scale, spatially dependent systematic errors. Precision supernova surveys (Betoule et al. 2014; Scolnic et al. 2018) and follow-up of optical transients from neutron star and black hole mergers (Abbott 2017; Anand et al. 2021) are just two examples of programs that require accurate corrections for extinction. The onslaught of accurate distances from Gaia and publicly available spectral and photometric data make future studies of the extraplanar extinction curve practical, while these applications make it pressing.

ORCID iDs

Ashley N. Piccone ● https://orcid.org/0000-0003-1233-1686
Henry A. Kobulnicky ● https://orcid.org/0000-0002-4475-4176

References

Aannestad, P. A. 1995, ApJ, 443, 653
Abbott, B. P. 2017, ApJL, 848, L12
Allard, F., Homeier, D., & Freytag, B. 2011, in ASP Conf. Ser., 448, 16th Cambridge Workshop on Cool Stars, Stellar Systems, and the Sun, ed. M. K. Browning & A. A. West (San Francisco, CA: ASP), 91
Anand, S., Coughlin, M. W., Kasliwal, M. M., et al. 2021, NatAs, 5, 46
Andersson, B. G., Lazarian, A., & Vaillancourt, J. E. 2015, ARA&A, 53, 501
Andersson, B. G., Pintado, O., Potter, S. B., Straižys, V., & Charcos-Llorens, M. 2011, A&A, 534, A19
Bailer-Jones, C. A. L., Rybizki, J., Fouesneau, M., Mantelet, G., & Andrae, R. 2018, AJ, 156, 58
Betoule, M., Kessler, R., Guy, J., et al. 2014, A&A, 568, A22
Bressan, A., Marigo, P., Girardi, L., et al. 2012, MNRAS, 427, 127
Cardelli, J. A., Clayton, G. C., & Mathis, J. S. 1989, ApJ, 345, 245
Castelli, F., & Kurucz, R. L. 2003, in Modelling of Stellar Atmospheres, Proc. of the 210th Symp. of the IAU, ed. N. Piskunov, W. W. Weiss, & D. F. Gray (San Francisco, CA: ASP), A20
Chambers, K. C., Magnier, E. A., Metcalfe, N., et al. 2016, The Pan-STARRS1 Surveys, arXiv:1612.05560
Choi, Y.-J., Min, K.-W., & Seon, K.-I. 2015, ApJ, 800, 132
Churchwell, E., Povich, M. S., Allen, D., et al. 2006, ApJ, 649, 759
Clark, S. E., Peek, J. E. G., & Putman, M. E. 2014, ApJ, 789, 82
Clayton, G. C., Wolff, M. J., Sofia, U. J., Gordon, K. D., & Misselt, K. A. 2003, ApJ, 588, 871
Cutri, R. M., Skrutskie, M. F., van Dyk, S., et al. 2003, VizieR On-line Data Catalog: II/246
Davis, L. J., & Greenstein, J. L. 1951, ApJ, 114, 206
Deharveng, L., Zavagno, A., Schuller, F., et al. 2009, A&A, 496, 177
Drimmel, R., Bucciarelli, B., & Inno, L. 2019, RNAAS, 3, 79
Ducati, J. R. 2002, CDS/ADC Collection of Electronic Catalogues
Fazio, G. G., Hora, J. L., Allen, L. E., et al. 2004, ApJS, 154, 10
Fernie, J. D. 1983, PASP, 95, 782
Fitzpatrick, E. L., Massa, D., Gordon, K. D., Bohlin, R., & Clayton, G. C. 2019, ApJ, 886, 108
Gehrz, R. D., Hackwell, J. A., & Jones, T. W. 1974, ApJ, 191, 675
Girardi, L., Bertelli, G., Bressan, A., et al. 2002, A&A, 391, 195
Gontcharov, G. A., & Mosenkov, A. V. 2019, MNRAS, 483, 299
Green, G. M., Schlafly, E., Zucker, C., Speagle, J. S., & Finkbeiner, D. 2019, ApJ, 887, 93
Gull, T. R., & Sofia, S. 1979, ApJ, 230, 782
Hall, J. S. 1949, Sci, 109, 166
Henden, A. A., Templeton, M., Terrell, D., et al. 2016, VizieR On-line Data Catalog: II/336
Henney, W. J., & Arthur, S. J. 2019, MNRAS, 486, 3423
Hiltner, W. A. 1949, Sci, 109, 165
Husser, T.-O., Wende-von Berg, S., Dreizler, S., et al. 2013, A&A, 553, A6
Jester, S., Schneider, D. P., Richards, G. T., et al. 2005, AJ, 130, 873
Johnson, H. L. 1965, ApJ, 141, 923
Jones, T. J., Stark, D., Woodward, C. E., et al. 2008, AJ, 135, 1318
Kim, S.-H., & Martin, P. G. 1996, ApJ, 462, 296
Kobulnicky, H. A., Chick, W. T., & Povich, M. S. 2019, AJ, 158, 73
Kobulnicky, H. A., Schurhammer, D. P., Baldwin, D. J., et al. 2017, AJ, 154, 201
Larson, K. A., & Whittet, D. C. B. 2005, ApJ, 623, 897
Larson, K. A., Wolff, M. J., Roberge, W. G., Whittet, D. C. B., & He, L. 2000, ApJ, 532, 1021
Lazarian, A., Goodman, A. A., & Myers, P. C. 1997, ApJ, 490, 273
Lazarian, A., & Hoang, T. 2007, MNRAS, 378, 910
Liszt, H. S., Pety, J., & Tachihara, K. 2009, A&A, 499, 503
Majewski, S. R., Zasowski, G., & Nidever, D. L. 2011, ApJ, 739, 25
Marshall, D. J., Robin, A. C., Reylé, C., Schultheis, M., & Picaud, S. 2006, A&A, 453, 635
Mathis, J. S., & Wallenhorst, S. G. 1981, ApJ, 244, 483
Oke, J. B. 1990, AJ, 99, 1621
Pecaut, M. J., & Mamajek, E. E. 2013, ApJS, 208, 9
Peek, J. E. G., & Schiminovich, D. 2013, ApJ, 771, 68
Reed, B. C. 2003, AJ, 125, 2531
Roulston, B. R., Green, P. J., & Kesseli, A. Y. 2020, ApJS, 249, 34
Santos, F. P., Chuss, D. T., Dowell, C. D., et al. 2019, ApJ, 882, 113
Schlafly, E. F., & Finkbeiner, D. P. 2011, ApJ, 737, 103
Schlafly, E. F., Peek, J. E. G., Finkbeiner, D. P., & Green, G. M. 2017, ApJ, 838, 36
Schlegel, D. J., Finkbeiner, D. P., & Davis, M. 1998, ApJ, 500, 525
Schmidt, G. D., Elston, R., & Lupie, O. L. 1992, AJ, 104, 1563
Schultz, G. V., & Wiemer, W. 1975, A&A, 43, 133
Scolnic, D. M., Jones, D. O., Rest, A., et al. 2018, ApJ, 859, 101
Serkowski, K., Mathewson, D. S., & Ford, V. L. 1975, ApJ, 196, 261
Siebenmorgen, R., Krełowski, J., Smoker, J., Galazutdinov, G., & Bagnulo, S. 2020, A&A, 641, A35
Sneden, C., Gehrz, R. D., Hackwell, J. A., York, D. G., & Snow, T. P. 1978, ApJ, 223, 168
Tachihara, K., Abe, R., Onishi, T., Mizuno, A., & Fukui, Y. 2000, PASJ, 52, 1147
Tielens, A. G. G. M. 2008, ARA&A, 46, 289

Tinbergen, J. 2005, Astronomical Polarimetry, 2005 (Cambridge: Cambridge Univ. Press)
Tody, D. 1986, Proc. SPIE, 627, 733
Turnshek, D. A., Bohlin, R. C., Williamson, R. L. I., et al. 1990, AJ, 99, 1243
van Dokkum, P. G. 2001, PASP, 113, 1420
van Leeuwen, F. 2007, A&A, 474, 653
Wardle, J. F. C., & Kronberg, P. P. 1974, ApJ, 194, 249

Whittet, D. C. B. 1977, MNRAS, 180, 29
Whittet, D. C. B., Gerakines, P. A., Hough, J. H., & Shenoy, S. S. 2001, ApJ, 547, 872
Wood, K., Haffner, L. M., Reynolds, R. J., Mathis, J. S., & Madsen, G. 2005, ApJ, 633, 295
Zacharias, N., Finch, C. T., Girard, T. M., et al. 2013, AJ, 145, 44